

Pair potentials for warm dense matter and their application to x-ray Thomson scattering in aluminum and beryllium

L. Harbour,^{1,*} M. W. C. Dharma-wardana,^{2,†} D. D. Klug,² and L. J. Lewis¹

¹*Département de Physique and Regroupement Québécois sur les Matériaux de Pointe, Université de Montréal, C.P. 6128, Succursale Centre-Ville, Montréal, Québec, Canada H3C 3J7*

²*National Research Council of Canada, Ottawa, Ontario, Canada K1A 0R6*

(Dated: November 14, 2018)

Ultrafast laser experiments yield increasingly reliable data on warm dense matter, but their interpretation requires theoretical models. We employ an efficient density functional neutral-pseudoatom hypernetted-chain (NPA-HNC) model with accuracy comparable to *ab initio* simulations and which provides first-principles pseudopotentials and pair-potentials for warm-dense matter. It avoids the use of (i) *ad hoc* core-repulsion models and (ii) “Yukawa screening”, and (iii) need not assume ion-electron thermal equilibrium. Computations of the x-Ray Thomson scattering (XRTS) spectra of aluminum and beryllium are compared with recent experiments and with density-functional-theory molecular-dynamics (DFT-MD) simulations. The NPA-HNC structure factors, compressibilities, phonons and conductivities agree closely with DFT-MD results, while Yukawa screening gives misleading results. The analysis of the XRTS data for two of the experiments, using two-temperature quasi-equilibrium models, is supported by calculations of their temperature relaxation times.

I. INTRODUCTION

High-energy deposition on matter using ultrafast lasers has opened the way to novel non-equilibrium regimes of density and temperature, raising issues of broad scientific interest [1]. These include hollow atoms, quasi-equilibrium solids and transient plasmas. The physics of warm dense matter (WDM) applies to hot carriers in nanostructures, space reentry, inertial confinement fusion [2, 3], Coulomb explosion, laser machining, surface ablation [4–6] and astrophysical environments, etc. The interactions in the WDM regime are characterized by the effective coupling parameter Γ , viz., the ratio of the Coulomb energy to the kinetic energy, which is bigger than unity. Simple approaches based on perturbation theory from a known “ideal” state thus become inapplicable.

Recent laser experiments on solid simple metals have reached WDM conditions through e.g., (i) ultrafast isochoric heating ($\rho = \rho_0$, where ρ_0 ρ are the initial and final densities, respectively) [7–9], and (ii) shock-compression ($\rho > \rho_0$) [10–14]. In situation (i) the optical laser directly interacts with a metallic target and couples to the free electrons causing their temperature T_e to reach many eV, while ions remain approximately at their initial temperature T_i . In situation (ii) the laser may pre-couple to the covalent electrons (bonds) of a non-metallic driver layer placed prior to the target material. This sets up a shock wave that can both heat and compress the target material which is usually metallic. If the driver layer is thick enough, the T_i attained by the target exceeds T_e as the shock wave does not directly couple to the electrons. A third and more complex situation (iii) arises if

the insulating driver layer creates a shock wave as before, but in addition the laser penetrates through it and deposits energy directly in the metallic target layer. The electron temperature T_e can then exceed the ion temperature T_i even in shock-compression experiments. Finally, the state of the WDM encountered by the probe beam also depends on the time delay τ_d between the pump laser and the probe laser [8, 15]. If τ_d significantly exceeds the electron-ion temperature relaxation time τ_{ei} , T_e and T_i would then relax to a common equilibrium temperature T . It should be noted that as T_e approaches T_i , the temperature relaxation becomes increasingly slower, and coupled-mode formation begins (on phonon timescales) and the process is further slowed down [15]. Hence the tacit assumption of thermal equilibrium in WDM created by laser-shock techniques can produce misleading interpretations of experiments, as we show in what follows.

In the discussion above we have assumed the simplest non-equilibrium paradigm, viz., the well-known two-temperature ($2T$) model [16]. However, this may be too simplistic. The laser may create spatial and thermal inhomogeneous distributions which are hard to interpret. On short timescales (e.g., <100 fs) or in more complex situations, even the electrons may not equilibrate to a common, unique temperature T_e [17].

X-ray Thomson scattering (XRTS) is a key method for studying WDM as it yields T_e , T_i , the ion density ρ , the mean electron density n_e , and details of ionic and electronic correlations. The XRTS signal is directly proportional to the total electron-electron dynamic structure factor $S_{ee}(k, \omega)$, which naturally follows a decomposition in terms of free-free, bound-bound and bound-free contributions from all “single ion sites”, as discussed by Chihara [18]. Such a decomposition is not available *directly* via density-functional theory (DFT) calculations, which use an N -ion simulation cell, since the electron density $n(r)$ calculated by such methods is the property of all the N ions. However, by combining DFT with molecular-

* Email address: louis.harbour@umontreal.ca

† Email address: chandre.dharma-wardana@nrc-cnrc.gc.ca

dynamics (MD) simulations (DFT-MD), the known ionic positions permit the calculation of the static ion-ion, ion-electron structure factors and the electron density at a “single ionic center”.

The work of Vorberger *et al.* [19] demonstrates the interest in simpler methods to obtain such ‘single-ion’ properties as charge densities $n(q)$ for WDM studies. In Ref. [19] $n(q)$ is calculated from an *externally obtained* pseudopotential (for Al). Since such potentials are not available for WDM conditions, the authors use an Ashcroft empty-core potential $U^{emp}(q)$ [20, 21]. However, such $U^{emp}(q)$ are applicable only for a few metals like Al at normal density and temperatures. The advantages and shortcomings of the empty-core pseudopotential even for aluminum at normal density and temperature are well known, and more complex transferable pseudopotentials are used in DFT-MD codes. The alternative of deconvoluting the N -ion charge density obtained from DFT-MD into a single-center charge density is a computationally demanding complex process. Instead, the neutral-pseudoatom (NPA) method directly constructs density- and temperature-dependent pseudopotentials *in situ* (without using transferable potentials) via an all-electron calculation. It is a rigorous DFT formulation that uses an *effective* single-ion model of the electron-ion system to provide all the required quantities directly in order to predict, say, the XRTS signal, with negligible computational cost. The only term that depends directly on T_i is the contribution to XRTS from the isotropic *ion feature* $W(k, \omega)$, sometimes referred to as the Rayleigh feature (see e.g. Refs. [22, 23]); it is given by

$$W(k, \omega) = |f(k) + q(k)|^2 S_{ii}(k, \omega), \quad (1)$$

$$S_{ii}(k, \omega) \simeq S_{ii}(k) \delta(\omega). \quad (2)$$

Here $f(k)$ and $q(k)$ are the form factors of bound $n_b(r)$ and free $n_f(r)$ electron densities *at an individual ion*, and $S_{ii}(k, \omega)$ is the dynamic structure factor of the ions. Current XRTS experiments cannot resolve ion dynamics (at meV energy scales); hence it is approximated by the static structure factor $S_{ii}(k)$, denoted hereafter as $S(k)$. Thus, while T_e and n_e are determined via the inelastic part of the XRTS signal, a determination of T_i is required to obtain the ion-ion $S(k)$.

Such computations of the XRTS signal have mostly been done with electronic-structure codes [24, 25] based on DFT Kohn-Sham calculations for a fixed set of N ions held in a simulation box, coupled with MD to move them and generate ensemble averages for observable properties. Results from these computationally intensive DFT-MD simulations are themselves fitted to intermediate quantities, e.g., simple “physically-motivated” pair potentials, to ease computations. Such intuitive models usually have hidden pitfalls but become entrenched as accepted practice unless corrected.

The objective of the present study is to employ the DFT-based NPA approach to provide simple first-principles calculations of the electron densities, $n(k)$, pseudo-potentials, $U_{ei}(k)$, and ion-ion pair interactions,

$V_{ii}(k)$. Here, by ‘first-principles’ we mean calculations that do not recourse to *ad hoc* intermediate models, but use only results flowing from the initial Kohn-Sham Hamiltonian of the NPA formulation. Admittedly, in calculating $S_{ii}(k)$ using an integral equation, a hard-sphere bridge parameter η is invoked. But it is determined by an optimization procedure internal to the method; or it may be avoided altogether by using MD with the NPA pair-potentials, as discussed below.

The pair-potentials when coupled with a hypernetted-chain (HNC) integral equation or MD yield structure factors $S(k)$ which can be used to calculate all other physical properties of WDM when used with the pseudopotentials and charge densities. In particular, all quantities needed for computing XRTS spectra, transport properties, energy relaxation, equation of state (EOS) etc., become available and may be used to investigate recent experiments as well as the quality of their interpretations employing popular “physically-motivated” *ad hoc* models. Since the NPA-HNC method is typically as accurate as DFT-MD, while orders of magnitude more efficient, it permits the rapid computation of $W(k)$ for several T_i in a very effective manner, enabling us to examine different $2T$ -models and their consistence with experiment.

In particular, the need for a simple potential has led to the use of an intuitive model that has come into vogue with WDM studies, viz. the “Yukawa + short-ranged repulsive (YSRR) potential” [10, 12, 26],

$$\beta_i V_{ii}^{\text{YSRR}}(r) = \sigma^4 / r^4 + \beta_i \exp(k_s r) / r, \quad (3)$$

introduced in Ref. [27]. Here, $\beta_i = 1/T_i$ is the inverse ion temperature, k_s is a screening wavevector and σ is a parameter fitted to MD data. We examine the validity of the YSRR approach using first-principles models and XRTS data for $2T$ systems ($T_e \neq T_i$) as well as for equilibrium systems. The YSRR potential is found to yield misleading conclusions about T_e and T_i , incorrect compressibilities (i.e., a property of the EOS), incorrect phonons and incorrect electrical conductivities.

The utility of the NPA-HNC and the possibility of two-temperature systems in laser-generated WDM is illustrated below by re-analyzing experiments on Al and Be. For Al, we examine shock-compressed systems by (i) Fletcher *et al.* [10] at $\rho/\rho_0 = 2.32$ and $T_e = 1.75$ eV and by (ii) Ma *et al.* [12] at $\rho/\rho_0 = 3.0$ and $T_e = 10$ eV with $\rho_0 = 2.7$ g/cm³; for Be, we examine the shock-compressed system by (iii) Lee *et al.* [13] at $\rho/\rho_0 = 2.99$ and $T_e = 13$ eV and the isochorically-heated system by (iv) Glenzer *et al.* [14] at $\rho/\rho_0 = 1$ and $T_e = 12$ eV with $\rho_0 = 1.85$ g/cm³.

II. THE NPA-HNC MODEL

An XRTS $W(k)$ calculation needs the electron density at an ion and the structure $S(k)$ of the system. The NPA approach [28–31] decomposes the total density

into a superposition of effective one-center densities combined *via* structure factors and provides a comprehensive scheme based on DFT. However, this is not intrinsically a superposition *approximation*; rather, this is a rigorous method in DFT which is often not recognized as such, with a tendency to consider it as a mean-field average-atom model. In effect, DFT provides a route to an *exact* average-atom description of an arbitrary electron-ion system. As discussed in Ref. [30], DFT asserts that the free energy $F[n, \rho]$ is a functional of the one-body electron density $n(\mathbf{r})$, and the one-body ion density $\rho(\mathbf{r})$, irrespective of the existence of complex interactions (e.g., superconductive associations for electrons), and complex covalent-bonding structure, *d*-bonds etc., for ions. Furthermore, the functional derivatives of $F[n, \rho]$ satisfy the following stationary conditions:

$$\delta F[n, \rho]/\delta n = 0, \quad (4)$$

$$\delta F[n, \rho]/\delta \rho = 0. \quad (5)$$

Standard DFT uses the first stationary condition to construct a Kohn-Sham one-body potential acting on an effective “one-electron” density $n(\mathbf{r})$. Similarly the stationary condition on the ion density, Eq. 5, defines a set of non-interacting “Kohn-Sham ions” moving in the classical form of the DFT potential acting on a “single ion” representative of $\rho(\mathbf{r})$. The ions can be regarded as classical spinless particles for our purposes. In Ref. [30] the potential acting on the “average ion” was identified with the “potential of mean-force” used in the theory of classical liquids [32]. Such an approach requires corrections beyond mean-field theory which are included in the exchange-correlation functional $F_{xc}^{ee}[n]$ for the electrons *and* in the ion-ion correlation functional $F_c^{ii}[\rho]$ for the ions. The ions are classical and do not have exchange (see Eq. 1.13, in Ref. [33]). Only pair-interactions between the DFT average-ions appear in the theory and the burden of approximating effects beyond pair-interactions falls on constructing these correlation functionals. It has in fact been shown that such an approach is successful even for liquid carbon with transient multi-center covalent bonding where carbon-carbon interactions are usually handled with multi-center “reactive bond-order potentials” [34].

However, here we study Al and Be in regimes where they are expected to be ‘simple liquids’. A sum of hypernetted-chain diagrams and bridge diagrams has been used to model $F_c^{ii}[\rho]$. The usual DFT-MD codes do not use Eq. 5 nor F_c^{ii} and F^{ei} since the ion many-body problem is not reduced to a one-body problem for the ions, unlike in the NPA. Instead, standard DFT uses a Born-Oppenheimer approximation where N ions in a simulation box are explicitly enumerated and provide an “external potential” to the Kohn-Sham electrons. In contrast, the NPA uses only the one-body ion distribution $\rho(\mathbf{r})$. Given a good ion-correlation functional $F_c^{ii}(\rho)$, enormous computational simplifications follow from this full-DFT approach compared to the standard method which calculates the Kohn-Sham eigenfunctions of a simulation cell containing typically $N = 64 - 128$ ions. Thus

the “single-center” NPA is a *rigorous* DFT average-atom approach, and its approximations lie in the construction of F_c^{ii} and F_{xc}^{ee} . The other advantage is that the NPA naturally provides “single-ion” properties like the mean ionization \bar{Z} , charge density $n(\mathbf{r})$ at a single ion, and the separation of the bound-electron and free-electron spectra (needed in XRTS theory) consistent with the exchange and correlation potentials used in the theory.

Several NPA models are described in the literature [35], e.g., those using ion-sphere models and other prescriptions not completely based on DFT theory. These different formulations affect how the chemical potential is treated and how the bound and free electrons are identified [31, 36–40]. We employ the NPA model of Perrot and Dharma-wardana [31, 41, 42] which includes a cavity of radius r_{ws} , with $r_{ws} = \{3/(4\pi\rho)\}^{1/3}$ the ion Wigner-Seitz radius, around the central nucleus to mimic, in a simplified way, the ion-density $\rho(r)$ of the plasma contained in a “correlation sphere” of radius $R_c \sim 10r_{ws}$. This is equivalent to using $(4/3)\pi(R_c/r_{ws})^3$, i.e., about 4200 particles in an MD simulations; in contrast, typical DFT-MD simulations use about 250 particles. The full ion distribution is subsequently evaluated by an HNC or modified-HNC (MHNC) procedure although MD may also be used, especially if low-symmetry situations are envisaged. The R_c is such that the pair-distribution functions (PDF), viz., ion-ion $g_{ii}(r)$ and ion-electron $g_{ie}(r)$ have asymptotically reached unity as $r \rightarrow R_c$. The electron-electron PDF g_{ee} can be shown to also reach the asymptotic limit when $r \rightarrow R_c$ as the e-e coupling is comparatively much weaker. The electron chemical potential is for non-interacting electrons at the interacting mean density n_e and temperature T_e , as required by DFT. The finite- T DFT calculations are done using a finite- T exchange-correlation functional F_{xc}^{ee} [43]. The free-electron density $n_f(r)$ is calculated using Mermin-Kohn-Sham wave functions which are orthogonal to the core states. Core-valence Pauli blocking, core-repulsions as well as core-continuum exchange-correlation effects are naturally included in the model. The NPA is an all-electron calculation and yields bound-state energies, bound-electron densities, as well as continuum densities and phase shifts which satisfy the Friedel sum rule.

The NPA free-electron pileup $n_f(k)$ around the NPA-nucleus is the key quantity in constructing electron-ion pseudopotentials $U_{ei}(k)$ and ion-ion pair potentials $V_{ii}(k)$, given in terms of the fully interacting static electron response function $\chi(k, T_e)$ as follows :

$$U_{ei}(k) = n_f(k)/\chi(k, T_e), \quad (6)$$

$$\chi(k, T_e) = \frac{\chi_0(k, T_e)}{1 - V_k(1 - G_k)\chi_0(k, T_e)}, \quad (7)$$

$$G_k = (1 - \kappa_0/\kappa)(k/k_{TF}); \quad V_k = 4\pi/k^2, \quad (8)$$

$$k_{TF} = \{4/(\pi\alpha r_s)\}^{1/2}; \quad \alpha = (4/9\pi)^{1/3}, \quad (9)$$

$$V_{ii}(k) = \bar{Z}^2 V_k + |U_{ei}(k)|^2 \chi_{ee}(k, T_e). \quad (10)$$

Here χ_0 is the finite- T Lindhard function, V_k is the bare Coulomb potential and G_k is a local-field correc-

tion (LFC). Hence the electron response goes beyond the random-phase approximation (RPA). The finite- T compressibility sum rule is satisfied since κ_0 and κ are the non-interacting and interacting electron compressibility, respectively, with κ matched to the F_{xc} used in the Kohn-Sham calculation. In Eq. 9, k_{TF} appearing in the LFC is the Thomas-Fermi wavevector. We use a G_k evaluated at $k \rightarrow 0$ for all k instead of the more general form (e.g., Eq. 50 in Ref. [43]) since the k -dispersion in G_k has negligible effect for the WDMs treated in this study. Note that the ‘‘Yukawa form’’ of the pair-potential is obtained from the above equations at sufficiently high temperatures since the Lindhard function can be approximated by its $k \rightarrow 0$ limit under such Debye-Hückel-like conditions, while G_k goes to zero. Such approximations are largely invalid in the WDM regime; Friedel oscillations in the pair-potentials contribute to defining the peak positions in the $g(r)$ and hence their relevance to observed properties is well-known experimentally and theoretically. Furthermore the need for finite- k screening instead of the Yukawa form is the norm for systems with $T/E_F < 1$ and normal densities. In fact the pair-potentials, PDFs, XRT features, conductivities and phonons will be incorrect if calculated from the $k \rightarrow 0$ Yukawa form for the given conditions. Hence all the observable properties studied here can be regarded as examples of observations of finite- k screening (see, e.g., Ref [44]).

The pseudopotential $U_{ei}(k)$ is a *local* potential which contains non-linear effects as the $n_f(k)$ was calculated from the Kohn-Sham equations. However, since it is forced to be linear in the response, the pair-potential Eq. 10 is trivially constructed. The regime of validity of this procedure is discussed in Ref. [45]. Outside the regime of validity it becomes increasingly more approximate, but as no *ad hoc* models extraneous to the calculation are invoked, it remains a first-principles method for constructing the pseudopotential from the all-electron single-center Kohn-Sham calculation. The structure factor $S(k)$ is computed (for uniform systems) from the modified hypernetted-chain (MHNC) equation which includes a bridge term $B(\eta, r)$ modeled using a Percus-Yevik hard-sphere fluid with a packing fraction η . The packing fraction is determined by the Lado-Foiles-Ashcroft *et al.* (LFA) criterion [46, 47] based on the Gibbs-Bogoluibov inequality. Although we use the MHNC equation, we refer to the general method as NPA-HNC, or occasionally as NPA-MHNC when we wish to emphasize the use of the MHNC procedure over the HNC one. It should also be noted that any ambiguity in the choice of the bridge function, or the use of a hard-sphere model for the bridge function, can be avoided if the NPA pair-potential is used directly in MD to generate $g(r)$. Such NPA+MD calculations were not deemed necessary in the present study.

Since the NPA pair-potential accurately predicts phonons (i.e., meV scales of energy) for common $2T$ WDM systems [48], even the dynamical $S_{ii}(\mathbf{k}, \omega)$ can be predicted when XRTS data at meV accuracy become

available. Furthermore, since all the PDFs and interaction potentials are available, the Helmholtz free energy F , and hence EOS properties, specific heats etc., as well as linear transport properties, can be calculated rapidly and in a parameter-free manner. Many such calculations have been presented in the past, as reviewed in Ref. [42]. Here we illustrate this for XRTS experiments on an equilibrium system and on a $2T$ -quasi-equilibrium system.

III. ALUMINUM

A. Shock-compressed Aluminum - I

Using XRTS, Fletcher *et al.* [10] have studied compressed aluminum evolving across the melting line into a WDM state (named Al-I hereafter). From their inelastic data, they determined the aluminum density and temperature to be $\rho/\rho_0 = 2.32$ and $T_e = 1.75$ eV, respectively. This density corresponds to a Wigner-Seitz radius $r_{ws} = 2.255$ a.u. for the ions and $r_s = 1.564$ a.u. for the electrons since the mean ionization \bar{Z} is found to be 3 from the NPA calculation. They used two 4.5 J laser beams on both sides of a 50 μm -thick Al foil coated with a 2 μm -thick layer of Parylene. A probe-pulse delay of $\tau_d = 1.9$ ns is used. Hence the assumption of thermal equilibrium ($T_e = T_i$) seems justified. The NPA free-electron charge density $n_f(r)$ at an Al^{3+} ion in the WDM system directly provides the pseudopotential U_{ei} and the pair-potential $V_{ii}^{\text{NPA}}(r)$. For the Yukawa screening of the YSRR potential, Fletcher *et al.* used the zero- T value of the Thomas-Fermi wavevector (Eq. 9). We find the value of σ to be 4.9 a.u., correcting what may be an error in Ref. [10] where $\sigma = 9.4$ a.u. is quoted [49]. The $S(k)$ corresponding to the NPA or the YSRR pair-potential can be calculated using an HNC or MHNC procedure, as appropriate, and used in Eq. 1 to compute the XRTS-signal $W(k)$.

In Fig. 1, the $W(k)$ computed from NPA and YSRR are compared with the experimental XRTS $W(k)$. In the NPA case, a bridge function $B(\eta, r)$ with $\eta = 0.354$ is obtained from the LFA criterion. The NPA-MHNC $W(k)$ is in good agreement with experiment and also confirms thermal equilibrium with $T_i = 1.75$ eV. No bridge correction is used for the YSRR since its $S(k \rightarrow 0)$ limit is already strongly inconsistent with the compressibility sum rule as will be illustrated below in the discussion (section III D). Since the conditions of the Fletcher experiment produce a near-degenerate electron gas ($T_e/E_F = 0.085$), the pair potential $V_{ii}^{\text{NPA}}(r)$ displays Friedel oscillations as can be seen in Fig. 2(a). The $S(k)$ from NPA-HNC and YSRR-HNC are shown in Fig. 2(b). The NPA-HNC $S(k)$ is very similar to the YSRR- $S(k)$ but differs in the $k \rightarrow 0$ region and near $2k_F$ (panel (c)), and this will affect some EOS properties.

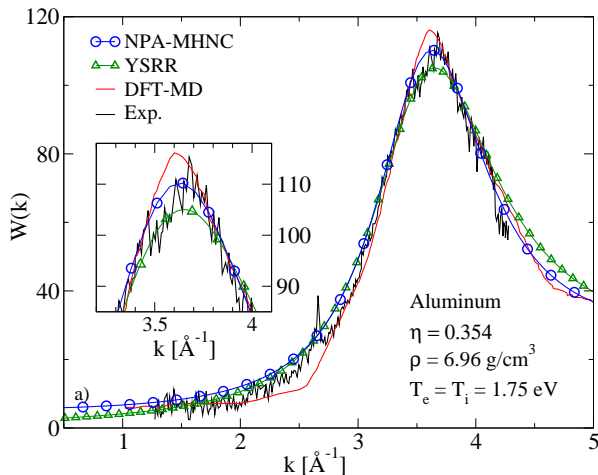


FIG. 1. The XRTS ion feature $W(k)$ of Ref. [10] for Al-I, and from the DFT-MD, NPA-MHNC and YSRR models, as indicated. The inset magnifies the peak region.

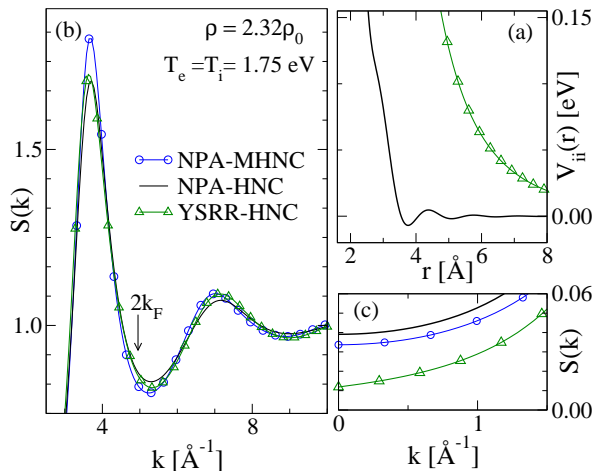


FIG. 2. (a) NPA and YSRR potentials for Al-I (cf. experiment of Ref. [10]); (b) $S(k)$ from the $V_{ii}(r)$ using HNC and MHNC; (c) $k \rightarrow 0$ region of $S(k)$.

B. Shock-compressed Aluminum-II

From inelastic data for shock-compressed Al (hereafter Al-II), Ma *et al.* [12] determined the experimental conditions in the target to be $\rho/\rho_0 = 3.0$ and $T_e = 10$ eV. This density corresponds to $r_{ws} = 2.07$ a.u. for the ions and $r_s = 1.435$ a.u. for the electrons. A set of nine pump beams, with a total energy of 4.5 kJ deposited in 1 ns, were aimed directly at the 125 μm -thick Al foil without any protective shield. The shock compression heats up the ion subsystem on the picosecond timescale, but the coupling of the laser to the free electrons in aluminum raises the electron temperature much more rapidly, within femtoseconds, creating a $2T$ -system with $T_i < T_e$ initially. If the data are collected after a sufficient time delay, an equilibrium temperature $T = T_i = T_e$ will be reached. Calculations using the YSRR potential with

$T_i = T_e = 10$ eV show good agreement with the XRTS ion feature. However, this turns out to be misleading since the ion feature of the system at $T_i = 10$ eV determined by the DFT-MD simulation of Rüter *et al.*[50] disagrees with the XRTS data of Ma *et al.* as shown at Fig. 3.

Using an “orbital-free” approach, viz. a Thomas-Fermi model with Weiszäcker corrections, Clérouin *et al.* [51] arrived at a $2T$ model with $T_i = 2$ eV and $T_e = 10$ eV in order to obtain good agreement with the XRTS data. They claimed that, since their method involves all electrons, the core-repulsion term included in the YSRR model is non-physical. Our NPA Kohn-Sham calculations — which are all-electron, parameter-free and include core and continuum states — confirm the conclusions of Clérouin *et al.* Using the NPA-potential for this case, a MHNC calculation with $\eta = 0.367$ predicts an excellent fit to the Ma *et al.* data with $T_i = 1.8$ eV and $T_e = 10$ eV, as can be seen in Fig. 3. In Fig. 4 (a)-(c), the NPA and YSRR $S(k)$, pair-potentials $V_{ii}(r)$ and the $k \rightarrow 0$ limit of $S(k)$ are shown. There are no Friedel oscillations in $V_{ii}^{\text{NPA}}(r)$ as T_e is nearly six times higher than in the conditions prevailing in Al-I. The disagreement between the NPA- $S(k)$ and the YSRR- $S(k)$ for $k \rightarrow 0$ should again be noted.

The high- k shoulders of the $W(k)$ curves from the $2T$ NPA-HNC and from the YSRR calculations are washed-out in the experiment, suggesting more complexity than in a $2T$ system. The ion subsystem may be cold (at 1.8 eV), but containing an unknown high- T component as well. On the other hand, it has been pointed out by Souza *et al.* [35] that the high intensity peak around $k \sim 4 \text{ \AA}^{-1}$ might be anomalous and caused by a non-Gaussian and/or broadened probe beam. The DFT-MD as well as the NPA results for the equilibrium case ($T_e = T_i = 10$ eV) both predict a peak height of ~ 65 , in strong contrast to the YSRR model, while the actual experimental peak height is ~ 106 .

Evidently, the XRTS data cannot be consistent with an equilibrium model. Since the aluminum target is pumped directly with a laser, the system would initially begin with $T_e > T_i$, and the possibility that the system has $T_e = 10$ eV, with the ion subsystem at $T_i \sim 2$ eV, is an entirely reasonable result. More complex non-equilibrium features [52] may also be envisaged, and may be useful for explaining the wings of the XRTS data. A model of the hot electrons involving a high-energy tail, energy bumps etc., would involve additional parameters that fit the observed $W(k)$, but without independent information to confirm them. Since the main XRTS $W(k)$ profile can be explained well within a $2T$ -model, this WDM is best regarded as being in a state with cold ions and hot electrons, but this by no means excludes more complicated situations which can be assessed only if more details of the experimental configuration and the pulsed heating process are available.

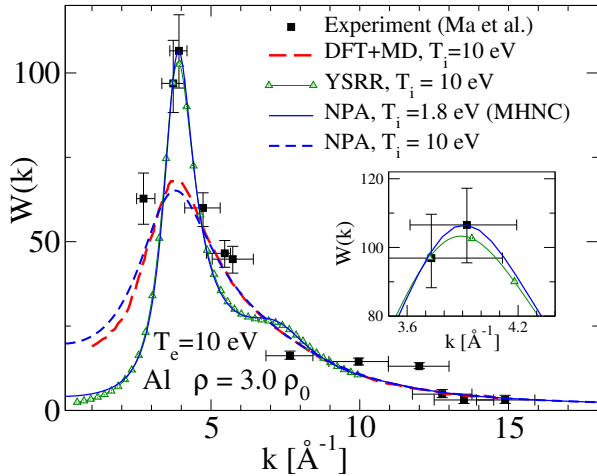


FIG. 3. The XRTS ion feature $W(k)$ of Ma *et al.* [12] for Al-II, compared with the $W(k)$ from YSRR, NPA, the DFT-MD calculation of Rütter *et al.* with $T_i = T_e$, and our $2T$ -NPA calculation with $T_i = 1.8$ eV and $T_e = 10$ eV; the inset magnifies the peak region.

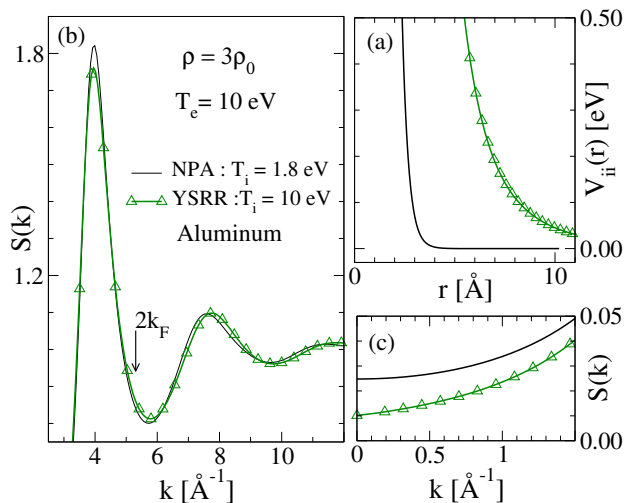


FIG. 4. (a) The NPA-HNC and YSRR pair potentials for Al-II; (b) corresponding $S(k)$; (c) the $k \rightarrow 0$ limit of $S(k)$.

C. Temperature relaxation in Al-II

In this section, our objective is to estimate the temperature relaxation time τ_{ei} in order to determine if the system has reached equilibrium within the pulse-probe delay. Assuming the $2T$ model with $T_e = 10$ eV and $T_i = 1.8$ eV, we can use the NPA electron-ion pseudopotential to calculate the temperature relaxation rate [15] via the Fermi Golden Rule (FGR). Since the FGR estimate of τ_{ei} was already sufficiently informative, we did not need a more detailed energy-relaxation model such as the coupled-mode description which is known to make the relaxation-time estimates somewhat longer. For this

purpose we define the form factor M_k of the pseudopotential by

$$M_k = U_{ei}(k)/\bar{Z}(Z_e V_k); \quad Z_e = -1. \quad (11)$$

The energy-relaxation rate, i.e., the rate of transfer of energy from the hot electrons to the ions per unit volume, calculated within a number of simplifying approximations, is given by

$$\frac{dE_e}{dt} = \omega_{i,p}^2 (T_e - T_i) \times \int \frac{d^3\vec{k}}{(2\pi)^3} V_k |M_{\vec{k}}|^2 \text{Im} \left[\frac{\partial}{\partial \omega} \chi^{ee}(\vec{k}, \omega) \right]_{\omega=0}, \quad (12)$$

where E_e is the energy in the hot electron subsystem at time t , $\omega_{i,p}$ is the ion plasma frequency and χ^{ee} is the fully interacting dynamic electron response function. The f -sum rule has been used to eliminate the dependence on the ionic structure [53] and hence provides an estimate of the energy relaxation which is superior to those obtained by using models for $S_{ii}(k, \omega)$, if the other assumptions made in the above theory hold. For instance, a difference of Bose factors of the form $N(\omega/T_e) - N(\omega/T_i)$, where $N(x) = 1/(\exp(x) - 1)$, for the density fluctuations in the electron system and the ion system respectively, has been approximated as $(T_e - T_i)/\omega$ in order to calculate a temperature relaxation rate. If T_i is assumed to be fixed (at least for a short timescale), we can use Eq. 12 for the energy relaxation rate of the electrons to determine a temperature relaxation rate. It requires a relation between the internal energy of an interacting warm-dense electron fluid and its temperature. Here we use the property that $F = F_0 + F_{xc}$, and the internal energy $E = \partial\{\beta F\}/\partial\beta$ as presented in Ref. [43] where the needed parametrizations are given. The replacement of the Bose factors by a temperature difference is not quite valid for the $T_i = 1.8$ eV and $T_e = 10$ eV estimated to prevail in the Ma *et al.* experiment since the electrons are partially degenerate.

Nevertheless, one can obtain a *grosso modo* estimate of the temperature-relaxation time τ_{ei} . It is found to be 300-400 ps depending on various assumptions. This timescale is sufficient for the formation of phonons, and hence the temperature relaxation towards equilibrium will be further slowed down by the formation of coupled modes (i.e., the conversion of ion-density fluctuations by electron screening into ion acoustic modes). This slows down the relaxation time by more than an order of magnitude. An actual estimate of the temperature relaxation of the target material (Al-II) will also have to account for the fact that the ion subsystem loses energy to its holding structure and the environment. These considerations independently support our conclusion, and that of Cl erouin *et al.*, that $T_i < T_e$ is a possible scenario, contrary to the ‘equilibrium model’ indicated by the YSRR model.

D. Discussion of Al results

DFT simulations treat the WDM sample as a periodic crystal made up of N nuclei whose positions in the simulation box evolve via MD and provide “single-electron” Kohn-Sham spectra. However, it provides no simple method for computing electron properties that can be attributed to a “single” nucleus, e.g., the mean ionization \bar{Z} arising from the bound and free parts of the spectrum, or pair interactions resulting from the single ions. The latter, if available, provides a convenient means of obtaining $S(k)$ and related properties of the WDM in a computationally efficient manner. The YSR model potential was justified by Wunsch *et al.* [27] as a suitable way of inverting a given $g(r)$ obtained from DFT-MD simulations in WDM conditions; it contains a Yukawa-like screening term based on an externally provided \bar{Z} and an explicit “core-repulsion” term.

The NPA approach rigorously constructs the effective Kohn-Sham “single-electron” density via the “single-ion” DFT description of the electron-ion system, as implied by the Euler-Lagrange equations given by Eq. 4 and Eq. 5. Thus, unlike DFT codes which treat the ions as an external potential, the NPA directly provides single-ion/single-electron properties as well as the pair potentials. The NPA calculation for Al-I, for the experiment of Fletcher *et al.*, shows that the mean radius of the $n = 2, l = 0$ bound shell in Al, which reflects the radius of the bound core, is 0.3552 Å. The YSR potential reaches large values already by 2 Å, i.e., at a radius nearly 6 times larger than the actual core size; thus the short-range repulsive part $(\sigma/r)^4$ is not appropriate. The claim in Ref. [10, 12] that the YSR potential “accounts for the additional repulsion from overlapping bound-electron wavefunctions” is certainly not confirmed by the shell structure of Al^{3+} in the plasma. Note that even the Wigner-Seitz radius, i.e., the sphere radius for an ion for aluminum at a compression of 2.32, is 2.255 a.u. = 1.193 Å, and hence the YSR model is clearly unphysical. The core-core interaction in Al can be calculated from the Al^{3+} core-charge density as in Appendix B of Ref. [54]. It is totally negligible for Al at compressions of 2.32 (in Al-I) or 3 (in Al-II) studied here. It should be noted that, as far as $S(k)$ is concerned, core-core interaction effects lead to an *attraction* due to core polarization, as was also discussed in Ref. [54]. This too can be neglected in aluminum.

The liquid-metal community of the 1980s found that the inverse problem of extracting a potential from the $S(k)$ given in a limited k -range, obtained from MD or from experiment, is misleading and not unique [55–57]. A parametrized physically-valid model (e.g., a pair potential $V_{ii}(r)$ constrained via an atomic pseudopotential) together with a good $B(\eta, r)$ [47] can successfully invert the MD data. However, the DFT-MD step is unnecessary in most cases since the $V_{ii}^{\text{NPA}}(r)$ and the $S(k)$ that provide the physics are easily evaluated from a rapid parameter-free NPA calculation. The YSR potential

is fitted to a limited range in r -space as in Wunsch *et al.* But the Fourier transform to obtain k -space quantities involves information on all of r -space. This leads to serious and uncontrolled errors unless a physically valid potential is used to extend the simulation $g(r)$ data to all r and hence to all relevant k . We note the following. (a) The YSR is proposed in Fletcher *et al.* for the computation of the EOS. Small- k behaviour is very important for EOS properties and we bring this out via the compressibility calculation. (b) Behaviour near $2k_F$ is important for transport and scattering processes and we bring this out via the resistivity calculation. (c) Other intermediate k -values are sampled by the phonons and we show that YSR fails for most- k in the phonon dispersion. Hence even when YSR ‘seems to work’ for one property, one cannot attribute any physical significance to it. Thus, besides the XRTS ion feature, we tested the validity of NPA and YSR models under WDM conditions by computing three key physical quantities, namely (i) compressibility κ , (ii) phonon spectra, and (iii) resistivity R , as we discuss below.

(i) To determine κ we assume that the sum rule $S(0) = \rho T_i \kappa$ holds for $2T$ systems under certain restrictions [58]. We computed κ using NPA, YSR and ABINIT, and obtained respectively 26, 9.6 and 30 a.u. for Al-I at a compression of 2.32 and $T_i = T_e = 1.75$ eV. The corresponding values for aluminum (Al-II) at a compression of 3, $T_i = 1.8$ eV and $T_e = 10$ eV, are 14, 1.1 and 16.4 a.u. In both cases, the results from the NPA are in close agreement with ABINIT whereas the YSR gives a much lower compressibility. Here, the YSR- $S(k)$ is calculated from the HNC without a bridge term, i.e. $B(\eta, r) = 0$, since a bridge term would make the compressibility even more erroneous. Thus, even in equilibrium, the YSR model is not trustworthy enough for EOS properties like the compressibility.

(ii) Even though the ionic system is clearly melted in both Al-I and Al-II conditions, a good test of the quality of the pair potential is the computation of the phonon spectrum for its low- T crystal structure (face-centered-cubic (FCC) for Al) which is a particular ionic configuration of the system even in the melt. In fact, the short-range structure of strongly coupled ionic fluids as reflected in the $S(k)$ is known to correspond closely to the $S(k)$ of the crystal structure below the melting point. The comparison of phonons obtained via the pair potential approach with those from *ab initio* calculations permits the validation of the energy landscape created by the pair potential for this particular ionic configuration. Such tests have already been done for other systems showing that the NPA predicts equilibrium and non-equilibrium phonons in good accord with *ab initio* simulations [48], which illustrates its meV-level of accuracy. The examination of phonon modes is relevant for ultra-fast-matter (UFM) studies where electron temperatures will rise significantly more rapidly than that of the nuclei. The limiting case where the nuclei are at low temperature is where phonon stability is relevant. The excellent agreement be-

tween the NPA and ABINIT longitudinal phonons in Al-I (Ref. [10]) and Al-II (Ref. [12]) is displayed in Fig 5 and further validates the NPA pair potentials in the WDM regime. The unphysical “stiffness” of the YSSR potential leads to high phonon frequencies and a sound velocity much larger than the NPA and ABINIT predictions.

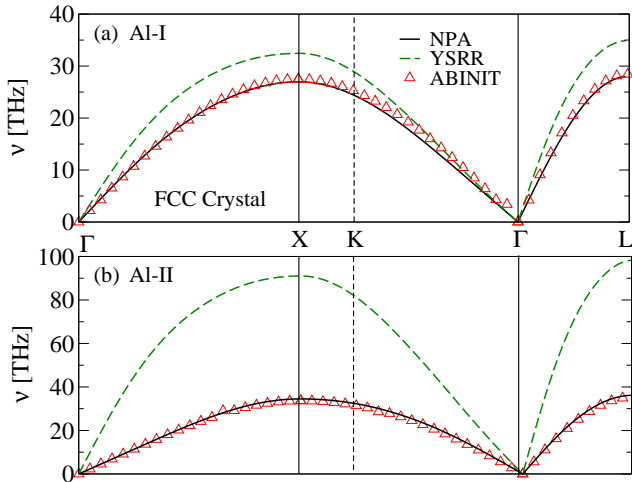


FIG. 5. The longitudinal phonon spectrum for the FCC crystal of a) Al-I, i.e. compression of 2.32 and $T_e = T_i = 1.75$ eV, Ref. [10]; b) Al-II, i.e. compression of 3.0, $T_i = 1.8$ eV, and $T_e = 10$ eV, Ref. [12]. The Γ , X, K and L point are symmetry points of the first Brillouin zone of the FCC crystal.

(iii) We tested the validity of the Yukawa component in the YSSR model and the validity of the YSSR- $S(k)$ by calculating the electrical resistivity R . The Yukawa pair potential $\bar{Z}^2 \exp(-k_s r)/r$ arises from the Yukawa pseudopotential $U_{ei}^y(q) = -4\pi\bar{Z}/q^2$ screened by the $k \rightarrow 0$ RPA dielectric function, i.e., $\epsilon(q) = 1 + (k_s/q)^2$. We use the Ziman formula in the form given in Ref. [54], Eq. (31) to calculate the resistivity. Computing R for the NPA and YSSR model, we obtain respectively 15.0 and 145 $\mu\Omega\cdot\text{cm}$ for Al-I while the corresponding values for Al-II are 9.65 and 99.4 $\mu\Omega\cdot\text{cm}$. Thus, in both cases, the resistivity predicted by the YSSR is about 10 times higher than the NPA value. Such larger-than-expected resistivities have also been obtained by Sperling *et al.*[9] while using an even simpler model than YSSR. The resistivities predicted by Sperling *et al.* are known to be in strong disagreement with the DFT-MD Kubo-Greenwood resistivity calculations of Sjoström *et al.* [59]. These issues are discussed at length in Ref. [60] where it is concluded that the Sperling calculation of the static conductivity is likely to be inapplicable. In Fig.6, we show that this behavior is also observed for various densities in equilibrium with $T = 1.75$ eV. The Ziman formula in conjunction with the NPA-HNC model, which includes a self-consistently generated $U_{ei}(k)$, $S(k)$ and a screening function $\chi(k)$ containing an LFC that satisfies the compressibility sum rule, is a well-tested method for many systems (for a review, see Ref. [42]) including aluminum [54, 61]. Thus, while it may be thought that additional *ab initio* or ex-

perimental resistivity data are required to confirm the NPA and Ziman formula results in the WDM regime, it is unlikely that the NPA resistivities are in error by an order of magnitude, given the excellent track record of NPA-resistivity predictions [61]. In our view, the Yukawa part of the YSSR calculation is responsible for the erroneous estimate of the resistivity.

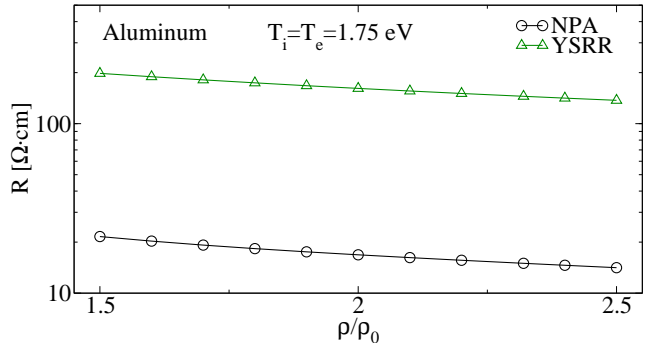


FIG. 6. The electrical resistivity of Al at $T = 1.75$ eV for different compressions calculated using NPA and YSSR.

In summary, through the calculation of phonons, compressibilities and resistivities, we showed that the short-ranged-repulsive and the Yukawa parts of the YSSR model are individually untenable. In contrast, the correct physics is quite simply obtained from the NPA-HNC for both the equilibrium and the $2T$ situation.

IV. BERYLLIUM

A. Shock-compressed Beryllium

Beryllium has been of recent interest (e.g., Ref. [62]) for many reasons including its potential applications as an ablator material in inertial-confinement fusion studies. Lee *et al.* [13] studied compressed beryllium by applying 12 pump beams, each with an individual energy of 480 J in 1 ns, directly on a 250 μm -thick Be foil without any coating. The pump-probe laser delay is ~ 4.5 ns, and may appear to be enough for electron-ion equilibration. We will examine this by a calculation of the τ_{ei} , as was done for aluminum. From an analysis of the XRTS data they concluded that Be is in a compressed state with $\rho/\rho_0 = 2.99$ and $T_e = 13$ eV (Be-I hereafter). Figure 7 compares the ion feature $W(k)$ from the NPA-HNC model with the experimental data of Ref. [13] and with the detailed and careful DFT-MD simulations of Plagemann *et al.* [63]. Even though NPA-HNC and DFT-MD do not predict exactly the same spectrum, both approaches agree in not confirming the first experimental point at $k = 1.3 \text{ \AA}^{-1}$ under the equilibrium condition $T_i = T_e = 13$ eV. By re-analyzing the original data (indicate as ‘Exp (re-fitted)’ in Fig. 7 and in Fig. 10), Plagemann *et al.* found that a $2T$ -system with $T_i = 9$ eV and $T_e = 13$ eV was able to repro-

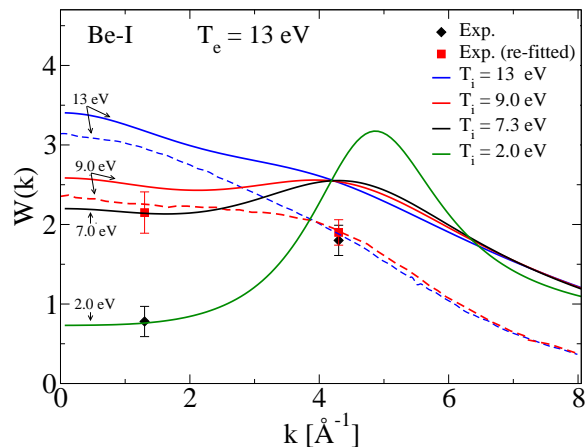


FIG. 7. The XRTS ion feature $W(k)$ of Lee *et al.* [13] compared with the NPA-HNC $W(k)$ (full lines) and with DFT-MD results (dashed lines) of Plagemann *et al.* [63] for equilibrium and for $T_e \neq T_i$, as indicated.

duce the spectrum. The NPA-HNC calculation does not predict the second experimental point at $k = 4.3 \text{ \AA}^{-1}$ as it shows higher values than DFT-MD for all values of k . To understand this difference between DFT-MD and NPA-HNC, we compared individually the two contributions to the ion feature, namely the static ion-ion structure factor $S(k)$ and the total electron form factor $N(k) = f(k) + q(k)$. In Fig. 8, a comparison of the $S(k)$ at different equilibrium temperatures shows excellent accord between NPA-HNC and DFT-MD. However, Fig. 9

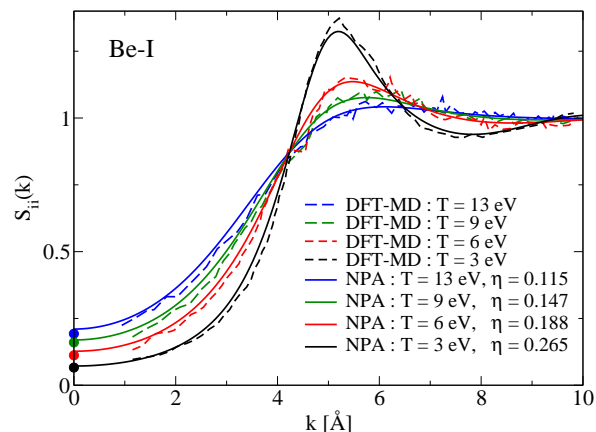


FIG. 8. Static ion-ion structure factor $S(k)$ for Be-I from the NPA-HNC and DFT-MD simulation of Plagemann *et al.* [63], including their $k = 0$ value marked as dots, for different equilibrium temperatures.

reveals important differences in the core-electron form factor $f(k)$ starting around $k = 4 \text{ \AA}^{-1}$. To determine $f(k)$, Plagemann *et al.* used snapshots of the DFT-MD simulation from the VASP code and post-processed in the ABINIT code using a “superhard” pseudopotential accounting for all four electrons. In contrast, NPA-HNC

is an all-electron atomic calculation including corrections from the ion environment which predicts an $f(k)$ similar to the independent pseudo-atom calculation of Souza *et al.* [35]. Since the discrepancy starts around $k = 4 \text{ \AA}^{-1}$, i.e., already deep into the core, it is possible that the “superhard” pseudopotential used does not reconstruct correctly the core electron density close to the nucleus. Further investigation should be done of this possibility which would account for the differences in the calculation of $W(k)$ from NPA-HNC and DFT-MD. Finally, using the NPA-HNC model while keeping $T_e = 13 \text{ eV}$, the best fit to the re-analyzed experimental $W(k)$ is obtained with $T_i = 7.3 \text{ eV}$ while it requires $T_i = 2 \text{ eV}$ to reproduce the original data. Given $T_i = 7 \text{ eV}$ and $T_e = 13 \text{ eV}$, the Be-target is better equilibrated than if one were to posit $T_i = 2 \text{ eV}$, and $T_e = 13 \text{ eV}$.

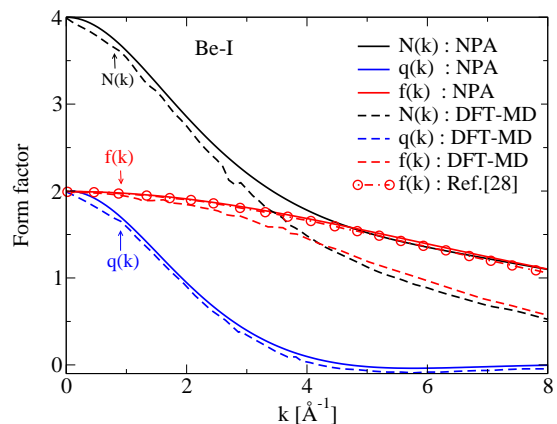


FIG. 9. Total $N(k)$, bound-electron $f(q)$ and free-electron $q(f)$ form factor for the Be-I conditions

B. Isochorically-heated Beryllium

Glenzer *et al.* [14] created an isochorically heated ($\rho/\rho_0 = 1$) WDM Be sample (named Be-II hereafter) by aiming 20 pump beams, with a total energy of 10 kJ over 1 ns, onto a 300 \mu m -thick Be cylinder coated by a protective 1 \mu m -thick silver layer. They determined that $T_e = 12 \text{ eV}$ while the pump-probe delay of 0.5 ns was considered sufficient to achieve thermal equilibrium between ions and electrons. In Fig. 10, the $W(k)$ from the NPA-HNC model is compared with the experimental data of Ref. [14] and with the DFT-MD simulations of Plagemann *et al.* [63]. The NPA-HNC and the DFT-MD calculations do not reproduce the original experimental data of Glenzer *et al.* nor the re-analyzed data using equilibrium conditions with $T_i = T_e = 12 \text{ eV}$. By keeping $T_e = 12 \text{ eV}$, Plagemann *et al.* found that it was possible to reproduce their (single) re-analyzed data point by setting $T_i = 6 \text{ eV}$. In order to reproduce this point, the NPA-HNC model requires a slightly lower ion temperature of $T_i = 5 \text{ eV}$. Within the NPA, it was impossi-

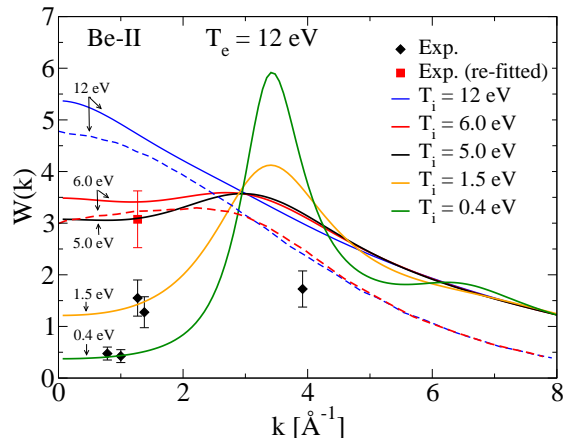


FIG. 10. The XRTS ion feature $W(k)$ of Glenzer *et al* [14] compared with the $W(k)$ of the NPA-HNC model (full lines) and with the DFT-MD simulation (dashed lines) of Plagemann *et al* [63] for the equilibrium and $2T$ situations.

ble to reproduce all four original experimental points for $k < 2\text{\AA}^{-1}$ with a single T_i . However, the first two points could be obtained with $T_i = 0.4$ eV while the two next points required $T_i = 1.5$ eV. Both models are not able to reproduce the point at $k = 3.9\text{\AA}^{-1}$ since it is too low to be reproduced with any T_i . As in the case of isochoric compressed Be studied by Lee *et al.* [13], the NPA-HNC model predicts higher $W(k)$ values than DFT-MD simulations for all k . A comparison between the NPA-HNC and the DFT-MD $S(k)$ is shown in Fig. 11, demonstrating close agreement between results from the NPA pair potential and DFT-MD. Hence, in this case also the difference in $W(k)$ between the two methods comes from the difference in the core electron form factor $f(k)$, which is essentially similar to the compressed-Be case presented in Fig. 9. Whether the “superhard” pseudopotential used by Plagemann *et al.* or other plasma effects included in the NPA treatment, but not in the DFT-MD, may be responsible for differences in the core electron density near the nucleus is unclear at present. We again note that the NPA is an “all-electron” method.

C. Discussion of Be results

In addition to the differences between NPA-HNC and DFT-MD in the $k > 4\text{\AA}^{-1}$ region for $W(k)$, we also observe a disparity at $k = 0$ for both Be systems studied here. Since the total electron form factor $N(k = 0) = 4$ is equal to the total number of electrons per ion, the divergence between the two models comes from the structure factor $S(k = 0)$ as shown in Figs. 9 and 11. It is very difficult to reach such low k values from DFT-MD simulations (because of the finite size of the simulation cell) and Plagemann *et al.* extracted them from independent thermodynamic calculations. As mentioned before, this quantity is important since it is linked to the compress-

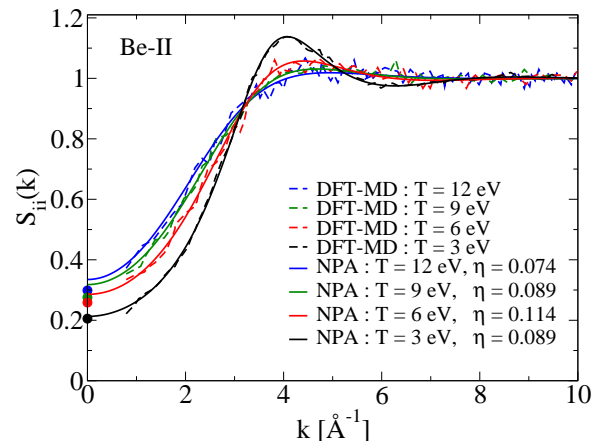


FIG. 11. Static ion-ion structure factor $S(k)$ for Be-II from the NPA-HNC model and from the DFT-MD simulations of Plagemann *et al* [63], including the $k = 0$ values marked as dots, for different equilibrium temperatures.

TABLE I. Compressibilities κ (in a.u.) of WDM beryllium calculated using DFT-MD and NPA-HNC.

System	Be-I (Ref. [13])	Be-II (Ref. [14])
T_i [eV]	13.0, 9.00, 6.00, 3.00	12.0, 9.00, 6.00, 3.00
κ (DFT-MD)	3.72, 4.47, 4.69, 5.54	18.6, 22.8, 32.1, 50.1
κ (NPA-HNC)	3.89, 4.73, 5.32, 6.01	20.8, 26.3, 35.5, 52.8

ibility κ via the sum rule $S(k = 0) = \rho T_i \kappa$. It should be noted that an accurate value of the compressibility κ should be determined from an EOS calculation, while the $S(k \rightarrow 0)$ limit, from an MHNC calculation, matches the EOS- κ only when the bridge contribution is optimal. Table I compares calculations from the NPA-HNC method and from DFT-MD by Plagemann *et al.* In both situations, the NPA-HNC compressibility is slightly higher than the DFT-MD, which is enough to affect the small- k region of the $W(k)$. This emphasizes the importance of experimental data for $k = 0$ in order to validate theoretical models and thermodynamics for WDM. On the other hand, we saw that, in the Be-II case, the two models are unable to predict the $k = 3.9\text{\AA}^{-1}$ data and that it is impossible to reproduce all four original experimental points for $k < 2\text{\AA}^{-1}$ using one single-ion temperature. The extraction of $W(k)$ is highly dependent on how the other terms in the Chihara decomposition, in particular the free-free electron-electron structure factor $S_{ee}^0(k, \omega)$, are computed. The $S_{ee}^0(k, \omega)$ is directly linked to the imaginary part of the response function χ and most authors have been using the Mermin [64] formulation while including electron-ion collisions in the Born approximation. It has been recently pointed out that the Mermin approximation is not applicable to UFM systems because of inherent assumptions behind the model [60]. Re-

cently, time-dependent-DFT-MD simulations have been done for Be [65] and it would be of interest to compare the total electron-electron dynamic structure factor $S_{ee}(k, \omega)$, including the bound-free contribution, in the WDM regime from these different models. Until a satisfactory model for $S_{ee}(k, \omega)$ is validated, it is hard to determine T_i via $W(k)$ but it should be kept in mind that a two-temperature system or other more complex situations might occur in laser-generated WDMs.

D. Temperature relaxation in Be

We consider the energy relaxation rate for the isochorically-heated beryllium (Be-II) where $\rho/\rho_0 = 1$, and for the particular $2T$ -case with $T_e = 12$ eV and $T_i = 6$ eV. Here the electron-sphere radius $r_s \simeq 1.92$ and T_e is close to the Fermi energy $E_F^{\text{Be-II}} = 16.6$ eV. Hence this system is far less degenerate than the Al-I and Al-II systems discussed above. The Fermi golden-rule calculation using the f -sum rule gives a temperature relaxation time of 150-200 ps. Coupled-mode formation may slow this down by an order of magnitude. Hence the claimed delay of about 500 ps may not be enough to achieve equilibration. The difficulties in matching the experimental data with simulations also indicate that we do not have a properly equilibrated WDM-Be sample.

In the case of the compressed Be sample with $T_e = 13$ eV (Be-I), the f -sum-based relaxation time is nearly five times faster than for Be-II. Hence temperature-equilibration shortcomings cannot be an explanation for the difficulties encountered in modeling the data using a $2T$ approach. Difficulties in reproducing the $W(k)$ using NPA-HNC and DFT-MD suggest that the experimental characterization requires further attention.

V. CONCLUSION

We have presented parameter-free all-electron NPA-HNC calculations of the charge densities, pseudo-potentials, pair potentials and structure factors that are required to interpret XRTS experiments. Compressibilities, phonons, resistivities as well as temperature-relaxation times for relevant cases have been presented, using the NPA pseudopotentials and structure factors where needed. Re-analyzing recent WDM experiments enabled us to (a) investigate the validity of the commonly-used YSRR model by showing that both its short-ranged part and its screening part yield misleading predictions; (b) expose pitfalls in inverting structure data to obtain effective pair potentials; (c) examine possible $2T$ -models and their temperature relaxation to examine the interpretations of $W(k)$ data from XRTS, emphasizing the need for caution in assuming thermal equilibrium in laser-generated WDM; and (d) demonstrate the accuracy of the NPA calculations of physical properties of electron-ion systems, from ambient temperatures and compressions to high temperatures and high compressions. The computational rapidity of the NPA-HNC model permits ‘on-the-fly’ testing-out of possible values of T_i, T_e and compressions that may rapidly fit an experiment, while this is time-consuming or impossible with DFT-MD simulations of properties like the ion feature $W(k)$ of WDM systems.

ACKNOWLEDGMENTS

This work was supported by grants from the Natural Sciences and Engineering Research Council of Canada (NSERC) and the Fonds de Recherche du Québec - Nature et Technologies (FRQ-NT). We are indebted to Calcul Québec and Calcul Canada for generous allocations of computer resources.

-
- [1] F. Graziani, M. P. Desjarlais, R. Redmer, SD. B. Trickey, *Frontiers and Challenges in Warm Dense Matter*, Springer, Berlin (2014)
 - [2] G. Dimonte and J. Daligault, Phys. Rev. Lett. **101**, 135001 (2008).
 - [3] F. R. Graziani *et al.*. Lawrence Livermore National Laboratory report, USA, LLNL-JRNL-469771 (2011).
 - [4] P. Lorazo, L. J. Lewis, and M. Meunier, Phys. Rev. Lett. **91**, 225502 (2003).
 - [5] D. Perez and L. J. Lewis, Phys. Rev. B **67**, 184102 (2003).
 - [6] Patrick Lorazo, Laurent J. Lewis, and Michel Meunier, Phys. Rev. B **73**, 134108 (2006);
 - [7] H. M. Milchberg, R. R. Freeman, S. C. Davey, and R. M. More, Phys. Rev. Lett. **61**, 2364 (1988).
 - [8] Z. Chen, B. Holst, S. E. Kirkwood, V. Sametoglu, M. Reid, Y. Y. Tsui, V. Recoules, and A. Ng, Phys. Rev. Lett. **110**, 135001 (2013).
 - [9] P. Sperling *et al.*, Phys. Rev. Lett. **115**, 115001 (2015).
 - [10] L. B. Fletcher *et al.*, Nature Photonics **9**, 274 (2015).
 - [11] E. García Saiz *et al.*, Nature **4** (2008).
 - [12] T. Ma *et al.*, Phys. Rev. Lett. **110**, 065001 (2013).
 - [13] H. J. Lee *et al.*, Phys. Rev. Lett. **102**, 115001 (2009).
 - [14] S. H. Glenzer *et al.*, Phys. Rev. Lett. **98**, 065002 (2007).
 - [15] M. W. C. Dharma-wardana, Phys. Rev. E **64**, 035432(R) (2001).
 - [16] S. I. Anisimov, B. L. Kapeliovich, and T. L. Perelman, Sov. Sov. Phys. JETP **39**, 375 (1974).
 - [17] N. Medvedev, U. Zastra, E. Forster, D. O. Gericke, and B. Rethfeld, Phys. Rev. Lett. **107**, 165003 (2011).
 - [18] J. Chihara, J. Phys. F : Met. Phys. **17**, 295-304 (1987).
 - [19] J. Vorberger and D. O. Gericke, Phys. Rev. E **91**, 033112 (2015)
 - [20] N. W. Ashcroft, Philos. Mag. **8**, 2055 (1963).
 - [21] N. W. Ashcroft, Phys. Lett. **23**, 48 (1966)
 - [22] S. H. Glenzer and R. Redmer, Rev. Mod. Phys. **81**, 1625 (2009).

- [23] G. Gregori, S. H. Glenzer, and O. L. Landen Phys. Rev. E **74** 026402 (2006).
- [24] G. Kresse and J. Furthmuller, Phys. Rev. B **54**, 11169 (1996).
- [25] X. Gonze *et al.*, Comp. Phys. Com. **180**, 2582-2615 (2009).
- [26] J. Ye, B. Zhao and J. Zheng, Phys. Plasma **4** 032701 (2011).
- [27] K. Wunsch, J. Vorberger, and D. O. Gericke, Phys. Rev. E **79**, 010201 (2009).
- [28] L. Dagens, J. Phys. C **5**, 2333 (1972).
- [29] L. Dagens, J. Phys. (Paris) **36**, 521 (1975).
- [30] M. W. C. Dharma-wardana and F. Perrot, Phys. Rev. A **26**, 4 (1982).
- [31] F. Perrot, Phys. Rev. E **47**, 570 (1993).
- [32] J.-P. Hansen and I. R. McDonald, *Theory of simple liquids* Academic Press, San Diego, (1990).
- [33] E. K. U. Gross, and Reinier M. Dreizler, *Density Functional Theory*, NATO ASI series, **337**,625 Plenum Press, New York (1993).
- [34] M. W. C. Dharma-wardana, arXiv:1607.07511 [cond-mat.stat-mech]
- [35] A. N. Souza, D. J. Perkins, C. E. Starrett, D. Saumon and S. B. Hansen, Phys Rev. E **89**, 023108 (2014).
- [36] C. E. Starrett and D. Saumon, Phys. Rev. E **92**, 033101 (2015).
- [37] Wilson *et al.*, JQSRT **99**, 658-679 (2006).
- [38] R. Piron and T. Blenski, Phys. Rev. E **83**, 026403, (2011).
- [39] A. Cangi and A. Pribram-Jones, Phys. Rev. B **92**, 161113(R) (2015).
- [40] M. S. Murillo, J. Weisheit, S. B. Hansen, and M. W. C. Dharma-wardana. Phys. Rev. E **87**, 063113 (2013).
- [41] F. Perrot and M.W.C. Dharma-wardana, Phys. Rev. E. **52**, 2920 (1995).
- [42] M. W. C. Dharma-wardana, Contr. Plasma Phys. **55** 97 (2015).
- [43] F. Perrot and M. W. C. Dharma-wardana, Phys. Rev. B **62**, 16536 (2000); *Erratum:* **67**, 79901 (2003); arXiv:1602.04734 (2016).
- [44] D.A. Chapman, J. Vorberger, L.B. Fletcher, R.A. Baggott, L. Divol, T. DoÃppner, R.W. Falcone, S.H. Glenzer, G. Gregori, T.M. Guylmer, A.L. Kritcher, O.L. Landen, T. Ma, A.E. Pak and D.O. Gericke, Nature Communications **6**, 6839 (2015).
- [45] M. W. C. Dharma-wardana, Phys. Rev. E **86**, 036407 (2012).
- [46] F. Lado, S. M. Foiles, and N. W. Ashcroft, Phys. Rev. A **28**, 2374 (1983).
- [47] H. C. Chen and S. K. Lai, Phys. Rev. A **45**, 3831 (1991).
- [48] L. Harbour, M. W. C. Dharma-wardana, D. D. Klug and L.J. Lewis, Contr. Plasma Phys. **55**, 144 (2015).
- [49] We have contacted the authors of Ref. [10] regarding this. If $\sigma = 9.4$, then the classical coupling constant at $r_{ws} = 1$ a.u. would be over 7800 at all temperatures as this term is independent of T . The HNC does not converge for $\sigma \sim 9$, although it may be treated using MD.
- [50] H. K. Rüter and R. Redmer, Phys. Rev. Lett. **112**, 145007 (2014).
- [51] J. Clérrouin, Grégory Robert, Philippe Arnault, Christopher Tricknor, Joel D. Kress, and Lee A. Colins Phys. Rev. E **91** 011101(R), (2015).
- [52] D. A. Chapman and D. O. Gericke, Phys. Rev. Lett, **107**, 165004 (2011).
- [53] G. Hazak, Z. Zinamon, Y. Rosenfeld, and M. W. C. Dharma-wardana, Phys. Rev. E **64** 035432(R) (2001).
- [54] François Perrot and M. W. C. Dharma-wardana, Phys. Rev E **52** 5352 (1995).
- [55] N. H. March, Canadian Journal of Physics, **65** 219-240, (1987).
- [56] M. W. C. Dharma-wardana and G. C. Aers Phys. Rev. B, **28**, 1701 (1983); Phys. Rev. Lett. **56**, 121 (1986).
- [57] Y. Rosenfeld and G. Kahl, Journal of Physics: Condensed Matter, **9**, L89 (1997)
- [58] Private communication, Th. Bonarth, R. Bredow and R. Redmer.
- [59] T. Sjostrom and J. Daligault, Phys. Rev E **92**, 063304 (2015)
- [60] M. W. C. Dharma-wardana, Phys. Rev. E **93**, 063205 (2016); arXiv:1602.04734 (2016).
- [61] J. F. Benage, W. R. Shanahan, and M. S. Murillo, Phys. Rev. Lett. **83**, 2953 (1999).
- [62] D. Li, H. Liu, S. Zeng, C. Wang, Z. Wu, P. Zhang and J. Yan, Nature Communications, Scientific reprints, **4** 5898 (2014)
- [63] K. Plagemann, H. R. Rüter, T. Bornath, M. Shihab, M. P. Desjarlais, C. Fortmann, S. H. Glenzer, and R. Redmer, Phys. Rev. E **92**, 013103 (2015).
- [64] N.D. Mermin, Phys. Rev. B **1**, 2362 (1970).
- [65] A. D. Baczewski, L. Shulenburg, M.P. Desjarlais, S.B. Hansen and R.J. Magyar, Phys. Rev. Lett. **116**, 115004 (2016)